PCCP

PAPER

View Article Online
View Journal | View Issue

Cite this: *Phys. Chem. Chem. Phys.*, 2018, **20**, 28511

Nonadiabatic fragmentation of H_2O^+ and isotopomers. Wave packet propagation using *ab initio* wavefunctions†

Jaime Suárez, ‡ L. Méndez and I. Rabadán *

Received 12th June 2018,
Accepted 16th September 2018

DOI: 10.1039/c8cp03725f

rsc.li/pccp

The fragmentation of the water cation from its $\tilde{B}\ ^2B_2$ electronic state, allowing the participation of the $\tilde{X}\ ^2B_1$, $\tilde{A}\ ^2A_1$ and $\tilde{C}\ ^2B_1$ states in the process, is simulated using the extended capabilities of the collocation GridTDSE code to account for the nonadiabatic propagation of wave packets in several potential energy surfaces connected by nonadiabatic couplings. Molecular data are calculated *ab initio*. Two initial wave packets are considered to reproduce two different experiments. The isotopic effect in the fragmentation of D_2O^+ and HDO^+ is also studied and the results show very good agreement with the experimental cleavage preference in the fragmentation of HDO^+.

1 Introduction

The water cation is naturally found in several environments such as the interstellar medium,[1,2] and atmospheres of planets[3] and comets.[4,5] It can be formed in collisions of electrons, ions or photons with H_2O and, given the importance of this molecule, many works have studied its ionization, and the ensuing dynamics of the remaining cation. Several experimental[6–8] and theoretical[9,10] works have addressed the photoionization of H_2O with photon energies below 21.2 eV. At these energies, the photoelectron spectrum shows three bands that correspond to the formation of H_2O^+ in the electronic states $\tilde{X}\ ^2B_1$ (hereafter denoted $\tilde{X}$), $\tilde{A}\ ^2A_1$ ($\tilde{A}$) and $\tilde{B}\ ^2B_2$ ($\tilde{B}$). These electronic states are essentially described by one-electron removal from the three outermost molecular orbitals ($1b_1$, $3a_1$ and $1b_2$, respectively) of H_2O. For photon energies higher than the dissociation threshold (18.1 eV), the vibrational levels of the $\tilde{B}$ state are predissociative and, accordingly, the third band of the H_2O photoelectron spectrum exhibits broad peaks. The ionization of H_2O above the dissociation threshold leads to the cation fragmentation into $H^+ + OH$, $H + OH^+$ and $O^+ + H + H$. Following the ionization of H_2O, coincidence experiments[11–14] have measured the branching ratios in the formation of $H^+ + OH$ and $H + OH^+$. Experiments of ref. 15–17 have measured the kinetic energy release distributions of the fragments formed after electron impact on water molecules, which shed light on the possible routes leading to the different fragmentation schemes.

Calculations on the H_2O^+ system include the *ab initio* studies[18,19] of the reactions $O + H_2^+ \rightarrow OH^+ + H$ and $O + H_2^+ \rightarrow OH + H^+$, and the corresponding reactions with the isotopomers D_2^+ and HD^+. These calculations used the quasi-classical-trajectory and real-wave-packet methods, and state-of-the-art potential energy surfaces of the $\tilde{X}$ and $\tilde{A}$ electronic states. The influence of the Renner–Teller coupling on the $O + H_2^+$ proton transfer reactions was analyzed in ref. 20.

In a previous paper,[21] we carried out a theoretical study of the fragmentation of the water cation from the $\tilde{B}$ state, obtaining values for the dissociation branching ratios into $OH + H^+$ and $H + OH^+$ that were in excellent agreement with the experimental data of Tan *et al.*[12] Our calculations consisted in nuclear wave-packet propagation on three electronic surfaces ($\tilde{B}$, $\tilde{A}$ and $\tilde{X}$), using a modified version of the GridTDSE code[22] to reproduce the nonadiabatic quantum nuclear dynamics. The initial condition of our dynamical calculation was the Franck–Condon (FC) wave packet, obtained by vertical ionization of the ground vibrational state of H_2O. The wave-packet propagation showed that the dissociation mechanism involves nonadiabatic transitions from the state $\tilde{B}$ to $\tilde{A}$ and $\tilde{X}$. The transition $\tilde{B}$–$\tilde{A}$ takes place in a few femtoseconds in the vicinity of the conical intersection (CI) between the corresponding potential energy surfaces (PESs). The CI seam appears at angles $\alpha \equiv \widehat{HOH}$ in the interval $60^\circ \lesssim \alpha \lesssim 100^\circ$, while the minimum of the $\tilde{A}$ PES is located at the linear geometry ($\alpha = 180^\circ$). As a consequence, the wave packet starts in $\tilde{B}$, moves towards the CI and is transferred to $\tilde{A}$ with an important excitation of the bending mode. At linear geometries, the states $\tilde{A}$ and $\tilde{X}$ become the two

Laboratorio Asociado al CIEMAT de Física Atómica y Molecular en Plasmas de Fusión, Departamento de Química, Universidad Autónoma de Madrid, Módulo 13, 28049-Madrid, Spain. E-mail: ismanuel.rabadan@uam.es

† Electronic supplementary information (ESI) available: A file containing the four adiabatic potential energy surfaces employed in the calculation is provided. See DOI: 10.1039/c8cp03725f

‡ Present address: Dipartimento di Chimica, Università degli Studi di Milano, 20133 Milano, Italy.

components of the $^2\Pi_u$ state, and the $\tilde{A}$–$\tilde{X}$ Renner–Teller (RT) interaction allows the population of the ground electronic state. The fragmentation can take place either by energy transfer from the bending mode into the antisymmetric stretching motion within $\tilde{A}$, leading to dissociation into $OH + H^+$, or after the RT transition between $\tilde{A}$ and $\tilde{X}$, leading to dissociation into $OH^+ + H$.

Although the good agreement between our results and the experimental branching ratios indicates that the three-state ($\tilde{B}$–$\tilde{A}$–$\tilde{X}$) mechanism explains the predissociation of the water cation, other possible nonadiabatic transitions must be ruled out. In our previous work,[21] we checked that the intersystem crossing transitions from $\tilde{B}$ and $\tilde{A}$ to the dissociative $\tilde{a}\ ^4B_1$ state are very slow compared to $\tilde{B}$–$\tilde{A}$ transitions. Here, we also consider the possible role of the $\tilde{C}\ ^2B_1$ ($\tilde{C}$) state in the wave packet evolution, because it exhibits a CI seam with $\tilde{X}$ at $\alpha = 180^\circ$ and relatively large O–H distances ($\approx$5 Bohr). Given the (large) internuclear distances at which this new CI is located, we have enlarged the grid of nuclear coordinates with respect to that of our previous calculation.

Additionally, we take advantage of the PESs and nonadiabatic data obtained for H_2O^+ to carry out a study of isotopic effects in the fragmentation of $D_2O^+(\tilde{B})$ and $HDO^+(\tilde{B})$. Our theoretical fragmentation branching ratios of D_2O^+ compare satisfactorily with the experimental results of Eland,[11] and they support the small differences found between H_2O^+ and D_2O^+ species in photoelectron–photoion-coincidence experiments.[13,14] With respect to HDO^+, time of flight coincidence experiments[23,24] in collisions of H^+ and F^{7+} with HDO have shown a strong preference for breaking the O–H bond after both single and double ionization of the molecular species. In those experiments, it was also found that the isotopic effect is independent of the projectile, suggesting a kinematic effect at play in the post-collisional breakdown of HDO^+ and HDO^{2+}. This interpretation was only supported by wave-packet simulations for HDO^{2+} in a single PES,[24] but one expects the fragmentation of HDO^+ to be dominated by transitions between several electronic states. Here, we study the isotopic dependence in the bond cleavage preference, by carrying out 4-PESs wave packet propagation for HDO^+.

In the (e–2e) + (e–e + ion) experiments of Tan *et al.*,[12] the ionization of H_2O is fast enough, compared to the characteristic rotational and vibrational periods of the molecule, that one can assume that the initial H_2O^+ wave packet is obtained by a FC transition from the ground state of H_2O. In this work, we also address the photodissociation experiments of Harbo *et al.*,[25] where the fragmentation starts from specific excited vibrational levels in $H_2O^+(\tilde{B})$. These authors carried out a crossed-beam experiment, where a H_2O^+ beam was crossed by a 532 nm laser. The subsequent dissociation was interpreted as due to the vibrational excitation of metastable low-lying vibrational levels of $\tilde{B}$. The experiment measured the ratio between the cross sections for production of the fragments $OH + H^+$ and $OH^+ + H$, obtaining a ratio value Γ:

$$\Gamma = \frac{\sigma(OH + H^+)}{\sigma(OH^+ + H)} = 1.3 \qquad (1)$$

in contrast with the value $\Gamma \approx 0.31$ reported by Tan *et al.*[12] The calculation of Γ with new initial conditions that simulate the experiment of Harbo *et al.* is a stringent test of both the electronic structure data and the dynamical methods employed.

The paper is organized as follows. In Section 2 we summarize the method employed to calculate the PESs and the dynamical couplings. The treatment of the two conical intersections found between $\tilde{B}$–$\tilde{A}$ and $\tilde{X}$–$\tilde{C}$ PESs, which are responsible for the nonadiabatic transitions, is discussed in Section 3. In Section 4, we describe the numerical method applied to solve the time-dependent Schrödinger equation. Our main results are shown in Section 5, which includes the results of a 4-state calculation using a FC initial wave packet, the isotopic effect and the calculations with initial conditions that are excited vibrational states of the $\tilde{B}$ state. A summary is presented in Section 6.

2 Electronic structure calculations

We have performed *ab initio* calculations for the electronic states $\tilde{X}\ ^2B_1$, $\tilde{A}\ ^2A_1$, $\tilde{B}\ ^2B_2$ and $\tilde{C}\ ^2B_1$ of H_2O^+ using the MOLPRO package.[26] PESs and nonadiabatic couplings have been obtained with multireference configuration interaction calculations in the C_s symmetry point group. Configurations are generated by allocating seven valence electrons in (7a′,1a″) molecular orbitals, previously obtained with CASSCF calculations in a space of (10a′,1a″) orbitals. The basis set employed is aug-cc-pvqz and aug-cc-pvtz[27] for oxygen and hydrogen, respectively.

In this paper, we use both internal (r_1,r_2,α) and Jacobi (r,R,θ) coordinates to describe the molecular geometry, as depicted in Fig. 1, where r_1 and r_2 are the O–H distances, α is the $\widehat{HOH}$ bond angle, R is the distance from the center of mass of the OH fragment to the remaining hydrogen, $r = r_1$, and θ is the angle between $\boldsymbol{r}$ and $\boldsymbol{R}$.

In our calculations, the equilibrium geometry of the neutral H_2O, in the ground state, is located at $r_e = r_1 = r_2 = 1.79$ Bohr and $\alpha_e = 104.6^\circ$ ($\theta_e = 107.8^\circ$). The equilibrium geometry of the ground state $\tilde{X}\ ^2B_1$ of H_2O^+ is also of C_{2v} symmetry, with no significant changes in the equilibrium coordinates ($r_e = 1.90$ Bohr and $\theta_e = 112.5^\circ$). In contrast, the equilibrium geometry of $\tilde{A}\ ^2A_1$ has $D_{\infty h}$ symmetry ($\alpha_e = 180^\circ$). The excited $\tilde{B}\ ^2B_2$ state is again of C_{2v} symmetry, but the r_e distance is 2.16 Bohr, larger than in the $\tilde{X}$ state, while the bond angle is $\theta_e = 80^\circ$, considerably smaller than in the $\tilde{X}$ state. These data, the energies of the corresponding potential energy minima and the dissociation energies, are given in Table 1.

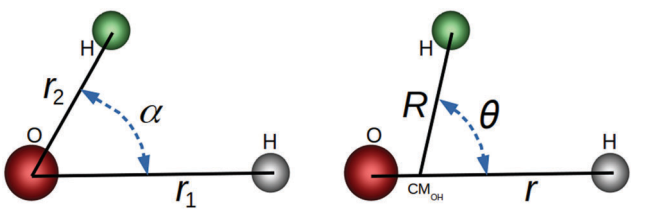

Fig. 1 Internal (left) and Jacobi (right) coordinates for the HOH nuclear framework.

Table 1 C_{2v} critical points of the first four electronic states of H_2O^+. The energy reference is taken as the minimum energy of the H_2O^+ ($\tilde{X}\ ^2B_1$)

State	r_e (Bohr)	α_e (deg.)	V_{min} (eV)	V_∞ (eV)	Fragments
$\tilde{X}\ ^2B_1$	1.90	110.0	0.0^{gm}	5.674	$OH^+ + H$
$\tilde{A}\ ^2A_1$	1.87	180.0	0.952^{gm}	6.245	$OH + H^+$
$\tilde{B}\ ^2B_2$	2.07	76.3	4.503^{gm}	7.850	$OH^+ + H$
$\tilde{C}\ ^2B_1$	3.10	90.0	10.572^{sp}	6.245	$OH + H^+$
$\tilde{C}\ ^2B_1$	2.87	180.0	7.850^{sp}		
$\tilde{C}\ ^2B_1$	3.42	30.0	7.388^{lm}		

gm: global minimum; lm: local minimum; sp: saddle point.

We show in Fig. 2 and 3 the contour plots of the PESs of the four adiabatic electronic states involved in the fragmentation dynamics. One can note the above-mentioned minima of the $\tilde{X}$ and $\tilde{A}$ surfaces. The changes in the slopes of the contour lines of the $\tilde{A}$ and $\tilde{B}$ surfaces at $\alpha \approx 80^\circ$ are due to the CI between these surfaces. At C_{2v} geometries, the $\tilde{C}$ surface shows two relatively shallow minima; the one at $\alpha = 180^\circ$ is a saddle-point in the (r,R)-plane, as seen in the bottom-right panel of Fig. 3.

In Fig. 4 we show the electronic energies of states $\tilde{X}$, $\tilde{A}$, $\tilde{B}$ and $\tilde{C}$ as functions of the Jacobi coordinate R, for fixed $r = 1.98$ Bohr, and four values of θ. In the panels corresponding to $\theta = 80^\circ$ and $\theta = 100^\circ$, the energy curve of state $\tilde{C}$ appears above those of states $\tilde{X}$ and $\tilde{A}$, and crosses state $\tilde{B}$ at energies with small weight in the initial FC wave packet, illustrated with Gaussian shade in the second panel. At $\theta = 170^\circ$, the states $\tilde{A}$ and $\tilde{X}$ are almost degenerate up to $r \simeq 5$ Bohr, where the potential energy curves of states $\tilde{C}$ and $\tilde{X}$ display an avoided crossing, that turns into a CI for $\theta = 180^\circ$.

3 Regularization of the conical intersections

The dynamical couplings are introduced in the numerical treatment by implementing a diabatic potential matrix in the grid representation. In fact, the nonadiabatic transitions take place in the neighbourhood of CIs, where the dynamical couplings are singular and, accordingly, a regularization procedure must be performed to remove these singularities. Given that the CIs are located in different regions of the configuration space, this regularization can be carried out for the CIs separately. The regularization procedure, already applied in our previous paper[21] to treat the CI between PESs $\tilde{A}$ and $\tilde{B}$ (henceforth referred as CI_1), uses the transformation angle:

$$\gamma_{ij} = \frac{1}{2}\tan^{-1}\left(\frac{2V_{ij}^{d}}{V_{jj}^{d} - V_{ii}^{d}}\right) \quad (2)$$

and the unitary transformation

$$\boldsymbol{U}(\gamma_{ij}) = \begin{pmatrix} \cos\gamma_{ij} & \sin\gamma_{ij} \\ -\sin\gamma_{ij} & \cos\gamma_{ij} \end{pmatrix} \quad (3)$$

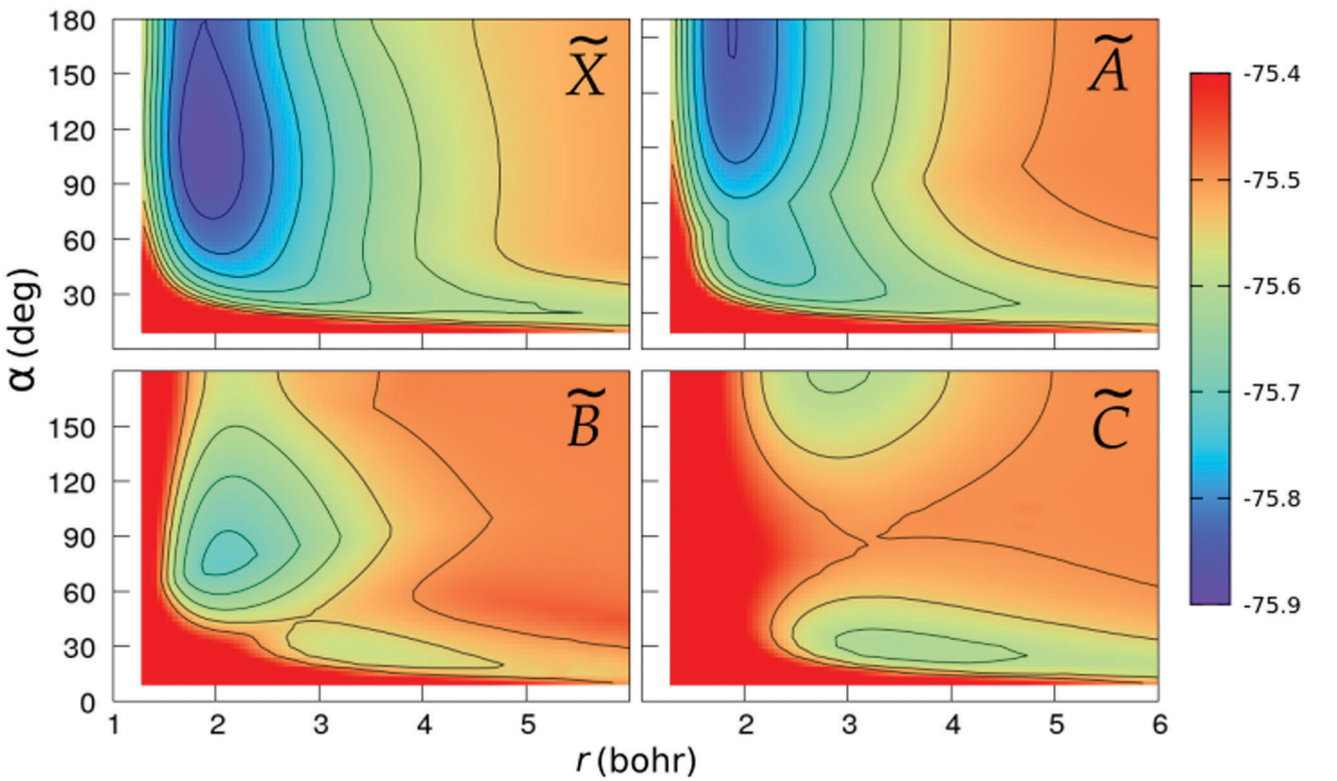

Fig. 2 Colour maps of the $\tilde{X}$, $\tilde{A}$, $\tilde{B}$ and $\tilde{C}$ PESs of C_{2v} geometries, as functions of the O–H distance r and the bond angle α. The numbers in the colour-box are energies in Hartree.

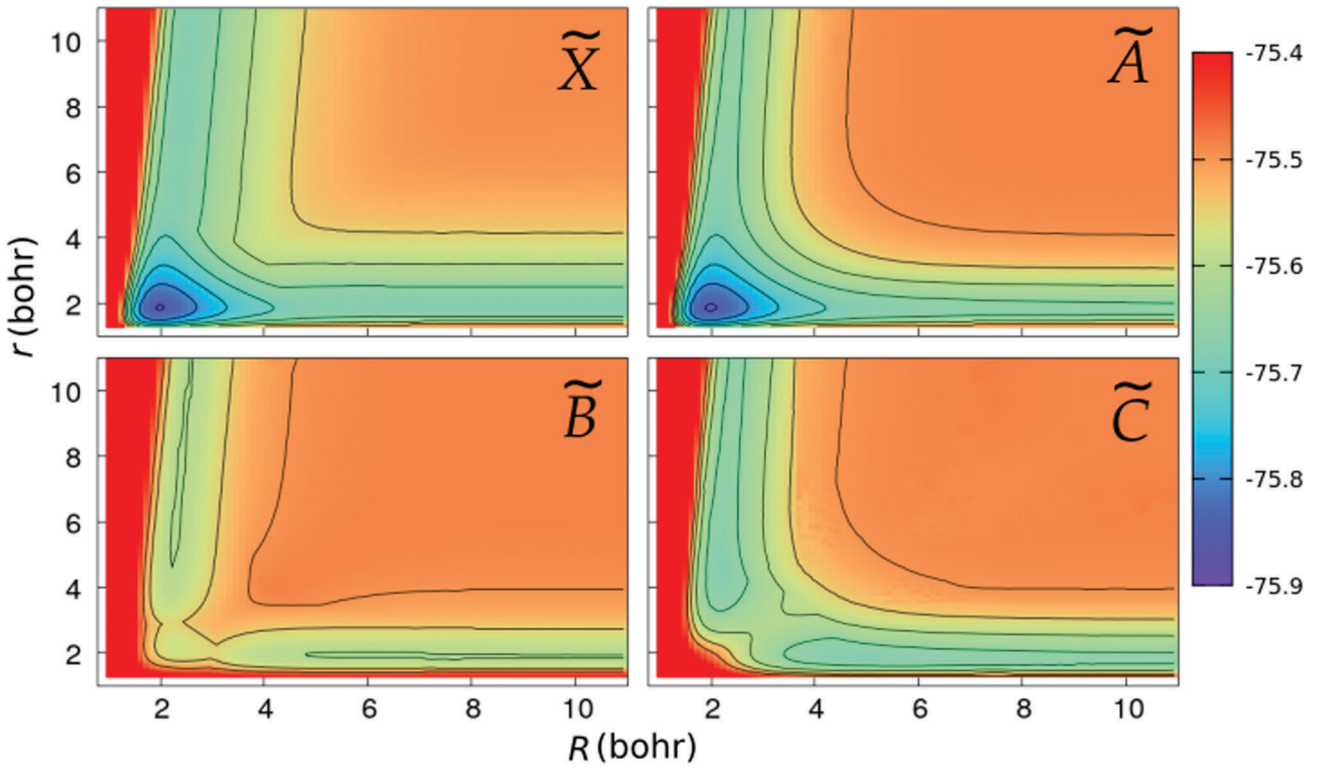

Fig. 3 Same as in Fig. 2, but for linear geometries and the PESs are plotted as functions of the Jacobi coordinates, r and R.

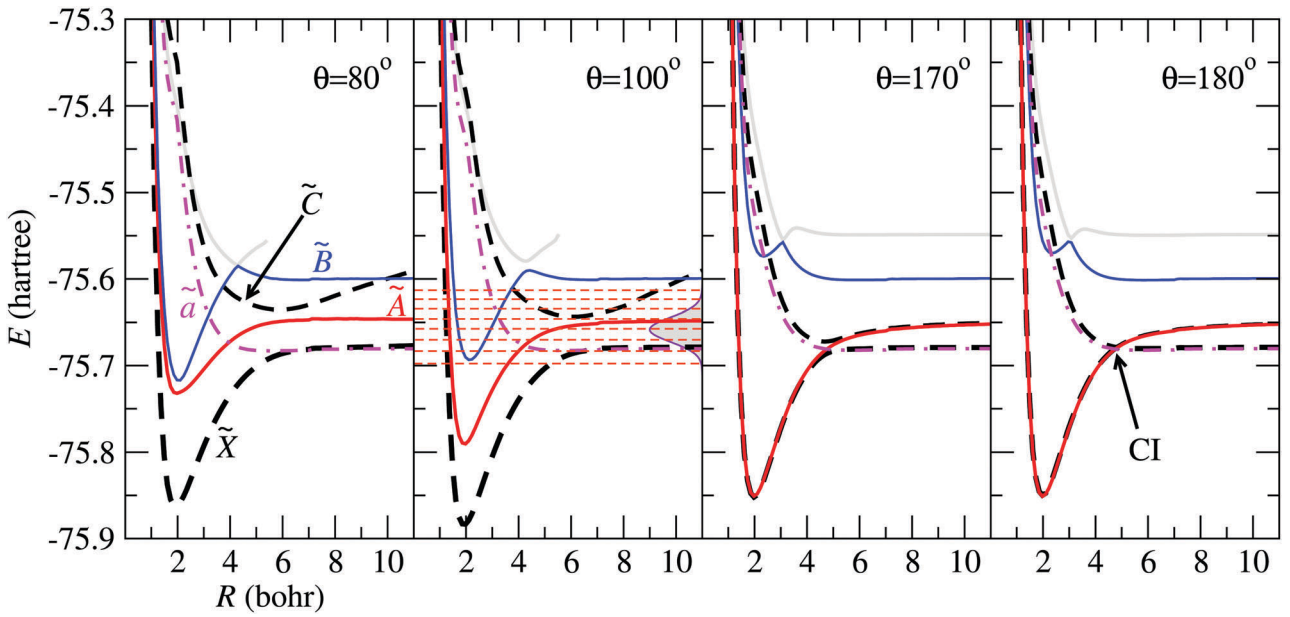

Fig. 4 Potential energy curves of the H_2O^+ system as functions of R for r = 1.98 Bohr and the values of θ indicated in the panels. The electronic states mentioned in the paper are labelled in the left panel, and the CI between $\tilde{X}$ and $\tilde{C}$ is indicated for θ = 180°. In the panel for θ = 100°, the energy distribution of the Franck–Condon wave packet is depicted with a Gaussian shaded area and the horizontal dashed-lines correspond to the vibrational energies in the adiabatic $\tilde{B}$ state.

to build the diabatic states $\boldsymbol{\chi}^{d} = \{\chi_i^{d}, \chi_j^{d}\}$ from the adiabatic ones $\boldsymbol{\chi}^{a} = \{\chi_i^{a}, \chi_j^{a}\}$:

$$\boldsymbol{\chi}^{d} = \boldsymbol{U}(\gamma_{ij})\boldsymbol{\chi}^{a} \quad (4)$$

The adiabatic potential energy surface matrix

$$\boldsymbol{V}^{a} = \begin{pmatrix} V_i^{a} & 0 \\ 0 & V_j^{a} \end{pmatrix} \quad (5)$$

is transformed into the diabatic potential matrix:

$$\boldsymbol{V}^{\mathrm{d}} = \begin{pmatrix} V^{\mathrm{d}}_{ii} & V^{\mathrm{d}}_{ij} \\ V^{\mathrm{d}}_{ji} & V^{\mathrm{d}}_{jj} \end{pmatrix} \tag{6}$$

by

$$\boldsymbol{V}^{\mathrm{d}} = \boldsymbol{U}(\gamma_{ij})\boldsymbol{V}^{\mathrm{a}}\boldsymbol{U}^{\dagger}(\gamma_{ij}) \tag{7}$$

For two-centre systems the adiabatic–diabatic transformation can be carried out to completely remove the radial couplings $\langle\chi^{\mathrm{d}}_i|\partial/\partial R|\chi^{\mathrm{d}}_j\rangle$. However, for any three (or more) centre system, the diabatic states do not exist. The scope of the regularization process is to find states with small couplings near the CIs, removing the singularities. In our calculation, this is accomplished by finding a transformation angle, γ_{ij}, that minimizes the nonadiabatic couplings between the diabatic states in the CI region. Explicitly, if Q is any particular nuclear coordinate, the residual coupling in the diabatic basis set is given by

$$\left\langle \chi^{\mathrm{d}}_i \middle| \frac{\partial}{\partial Q} \middle| \chi^{\mathrm{d}}_j \right\rangle = \left\langle \chi^{\mathrm{a}}_i \middle| \frac{\partial}{\partial Q} \middle| \chi^{\mathrm{a}}_j \right\rangle - \frac{\partial \gamma_{ij}}{\partial Q} \tag{8}$$

As seen in ref. 21, the Ã–B̃ CI takes place along a seam of C_{2v} geometries, and the regularization is more easily carried out by employing the symmetry coordinates $\{x,y,\alpha\}$

$$x = \frac{r_1 + r_2}{2}; \quad y = \frac{r_1 - r_2}{2} \tag{9}$$

built from the internal coordinates r_1 and r_2 (see Fig. 1). In these coordinates, our calculations indicate that a CI seam is located at $y = 0$ for angles (in radians):

$$\alpha_{\mathrm{CI}_1}(x) = \frac{1.43x}{1 + 0.61x} \tag{10}$$

The transformation angle $\gamma_{\tilde{\mathrm{A}}\tilde{\mathrm{B}}}$ is written in terms of the internal coordinates, and, similar to previous works,[28,29] the energy difference $\Delta V_{\tilde{\mathrm{A}}\tilde{\mathrm{B}}} = V^{\mathrm{d}}_{\tilde{\mathrm{B}}\tilde{\mathrm{B}}} - V^{\mathrm{d}}_{\tilde{\mathrm{A}}\tilde{\mathrm{A}}}$ is taken proportional to the distance to the CI seam in the $y = 0$ plane. As $\alpha_{\mathrm{CI}_1}{}' = \mathrm{d}\alpha_{\mathrm{CI}_1}/\mathrm{d}x$ is small in the range of x where the interaction is sizable, the energy difference can be approximated by

$$\Delta V^{\mathrm{d}}_{\tilde{\mathrm{A}}\tilde{\mathrm{B}}}(x) = [\alpha(x) - \alpha_{\mathrm{CI}_1}(x)]\cos(\alpha_{\mathrm{CI}_1}{}') \tag{11}$$

The interaction term is proportional to the antisymmetric coordinate y, including a dependence on α that gives an extra flexibility to the transformation angle to minimize the residual couplings:

$$V^{\mathrm{d}}_{\tilde{\mathrm{A}}\tilde{\mathrm{B}}}(\alpha,y) = (a_0 + a_1\alpha + a_2\alpha^2)y \tag{12}$$

where the values of the a_i parameters are given in Table 2.

Table 2 Parametrization used for CI_1 (eqn (12)) and CI_2 (eqn (13), (17) and (18)). The constants are expressed in atomic units

i	a_i	b_i	c_i	d_i
0	2.21	−0.0692	2.82	−1.57
1	0.94	1.11	0.367	−0.245
2	−2.88	2.25	−0.693	

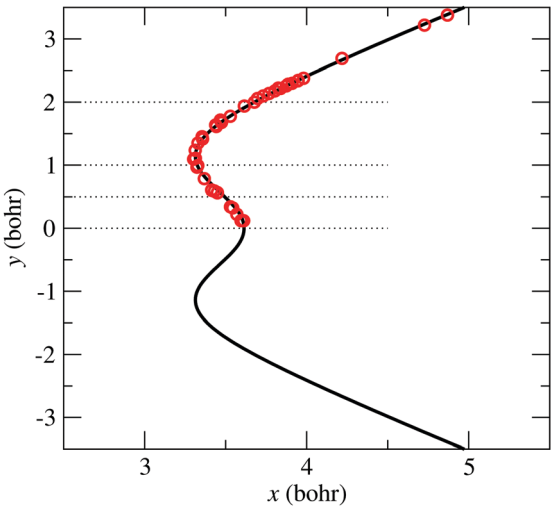

Fig. 5 Bullets: position in coordinates (x, y), eqn (9), of the zero-energy differences between states X̃ and C̃ at $\alpha = \pi$ rad. Solid-line: CI_2 seam fitted-model of eqn (13).

The second CI considered (CI_2, henceforth) takes place between PESs X̃ and C̃ at angles $\alpha \approx \pi$.

The symbols in Fig. 5 indicate the coordinates of the geometries with zero-energy difference between states X̃ and C̃. The position of the seam in the (x,y) plane is parametrized using the following expression:

$$x_{\mathrm{CI}_2}(\alpha,y) = f_0(\alpha) + \frac{f_1(\alpha)y^2}{f_2(\alpha) + |y|} + \mathrm{e}^{-y^2} \tag{13}$$

in which the values of f_i are obtained by a non-linear least-square fitting procedure of the previous equation to the points of minimum energy difference for eight values of α. The $f_i(\alpha)$ functions are fitted, independently, to the following expressions:

$$f_0(\alpha) = b_0\alpha + c_0 \tag{14}$$

$$f_1(\alpha) = b_1\,\mathrm{e}^{-c_1(\alpha-\pi)^2} \tag{15}$$

$$f_2(\alpha) = b_2\,\mathrm{e}^{-c_2(\alpha-\pi)^2} \tag{16}$$

Again, b_i and c_i parameters are obtained by a 1D-non-linear fitting procedure, and are given in Table 2.

The modelled diabatic potential matrix elements are finally written as

$$\Delta V^{\mathrm{d}}_{\tilde{\mathrm{X}}\tilde{\mathrm{C}}}(\alpha,x,y) = x - x_{\mathrm{CI}_2}(\alpha,y) \tag{17}$$

$$V^{\mathrm{d}}_{\tilde{\mathrm{X}}\tilde{\mathrm{C}}}(\alpha,y) = d_0\,\mathrm{e}^{d_1y^2}(\alpha - \pi) \tag{18}$$

where d_0 and d_1 are also free parameters obtained by non-linear fitting of this model to the *ab initio* couplings $\langle\psi_{\tilde{\mathrm{X}}}|\partial/\partial x|\psi_{\tilde{\mathrm{C}}}\rangle$, for several values of y, and whose values are given in Table 2.

The X̃–C̃ seam described by eqn (13) is plotted in Fig. 5, together with the position of the *ab initio* zero-energy difference between these states for linear geometries. Also, in Fig. 6, we compare, for $\alpha = 175^\circ$, the *ab initio* nonadiabatic couplings (symbols) with the values of the derivatives (solid lines) of the transformation angle $\gamma_{\tilde{\mathrm{X}}\tilde{\mathrm{C}}}$ [see eqn (2)] obtained with the fitted model (17) and (18), for a few values of y (those corresponding

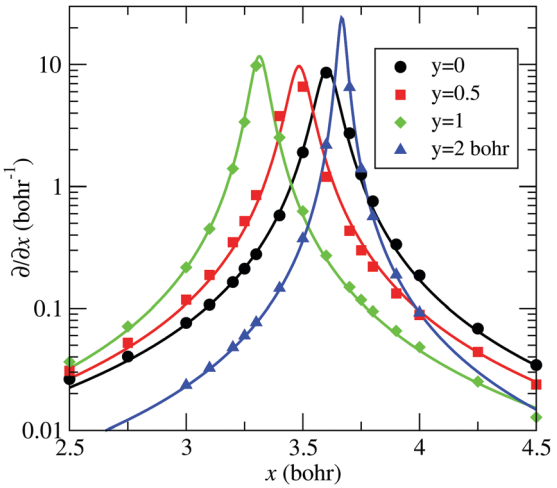

Fig. 6 Comparison between *ab initio* $\langle\Psi_{\tilde{X}}|\partial/\partial x|\Psi_{\tilde{C}}\rangle$ (symbols) and the model of eqn (13) $\partial\gamma_{\tilde{X}\tilde{C}}/\partial x$ (solid-lines) as functions of x, for various values of y, labelled in the graph, and also indicated with dotted lines in Fig. 5. Modelled and *ab initio* data were obtained with $\alpha = 175°$.

to the dotted lines of Fig. 5). These figures show the satisfactory fitting of the model to the *ab initio* data, where the peaks of the lorentzian follow the location of the CI_2 seam and their widths depend on the parameters of eqn (18). A more global view of the topology of the CI_2 is shown in Fig. 7, where we plot the derivative of the transformation angle $\gamma_{\tilde{X}\tilde{C}}$ with respect to the symmetry coordinates $\{x,y,\alpha\}$. These derivatives mimic the behaviour of the nonadiabatic couplings between the states $\tilde{X}$ and $\tilde{C}$ near their CI.

The treatment of $\tilde{A}$–$\tilde{X}$ transitions, explained in our previous paper, is based on the method of Haxton *et al.*[30,31] that yields a couple of diabatic states. Assuming a small total angular momentum, the Coriolis coupling terms are neglected and the body-fixed nuclear Hamiltonian has the form, in Jacobi coordinates:[31,32]

$$\begin{aligned} H &= V(R,r,\theta) - \frac{1}{2\mu_R R}\frac{\partial^2}{\partial R^2}R - \frac{1}{2\mu_r r}\frac{\partial^2}{\partial r^2}r \\ &\quad - \frac{1}{2}\left(\frac{1}{\mu_R R^2} + \frac{1}{\mu_r r^2}\right) \\ &\quad \times \left(\frac{1}{\sin\theta}\frac{\partial}{\partial\theta}\sin\theta\frac{\partial}{\partial\theta} - \frac{j_z^2}{\sin^2\theta}\right) \end{aligned} \tag{19}$$

where j_z is the z component of the angular momentum operator for the rotation of the diatom OH in the body-fixed frame, with $\boldsymbol{R}$ along the $\hat{z}$-axis. In this approximation, the nuclear wave functions are assumed to be eigenfunctions of the body-fixed operator j_z. The operator ${j_z}^2$ is substituted[33] into eqn (19) by its eigenvalue, k^2 ($k = K - M_L$), which is only defined in the $C_{\infty v}$ or $D_{\infty h}$ symmetries, where K and M_L are the quantum numbers for the z projections of the total and electronic angular momenta, respectively. In the present case, the electronic states $\tilde{A}\ ^2A_1$ and $\tilde{X}\ ^2B_1$ correlate, in the limit $\theta \to 180°$, with the two components of the $^2\Pi_u$ state, both with $\Lambda = |M_L| = 1$. In this limit, the $\chi_{\pm1}$ eigenfunctions of L_z with $M_L = \pm1$ are linear combinations of the electronic wave functions, $\chi_{\tilde{A}}$ and $\chi_{\tilde{X}}$:

$$\chi_{\pm} = \frac{1}{\sqrt{2}}(\chi_{\tilde{A}} \pm i\chi_{\tilde{X}}) \tag{20}$$

These two combinations are employed for all values of θ. Considering the transformations due to the regularization of the two CIs and the transformation (20), the unitary matrix, $\boldsymbol{U}$, for the transformation from the adiabatic state vector $\boldsymbol{\chi}^a = \{\chi^a_{\tilde{C}},\chi^a_{\tilde{X}},\chi^a_{\tilde{A}},\chi^a_{\tilde{B}}\}$ to the diabatic one $\boldsymbol{\chi}^d = \{\chi^d_{\tilde{C}},\chi_+,\chi_-,\chi^d_{\tilde{B}}\}$ is

$$\boldsymbol{U} = \begin{pmatrix} \cos\gamma_1 & \frac{-i}{\sqrt{2}}\sin\gamma_1 & \frac{i}{\sqrt{2}}\sin\gamma_1 & 0 \\ -\sin\gamma_1 & \frac{-i}{\sqrt{2}}\cos\gamma_1 & \frac{i}{\sqrt{2}}\cos\gamma_1 & 0 \\ 0 & \frac{1}{\sqrt{2}}\cos\gamma_2 & \frac{1}{\sqrt{2}}\cos\gamma_2 & -\sin\gamma_2 \\ 0 & \frac{1}{\sqrt{2}}\sin\gamma_2 & \frac{1}{\sqrt{2}}\sin\gamma_2 & \cos\gamma_2 \end{pmatrix} \tag{21}$$

with $\gamma_1 \equiv \gamma_{\tilde{X}\tilde{C}}$ and $\gamma_2 \equiv \gamma_{\tilde{A}\tilde{B}}$. $\boldsymbol{U}$ relates the adiabatic, $\boldsymbol{V}^a$, and diabatic, $\boldsymbol{V}^d$, potentials:

$$\boldsymbol{V}^d = \boldsymbol{U}\boldsymbol{V}^a\boldsymbol{U}^\dagger \tag{22}$$

4 Computational dynamics

The dynamical calculation has been carried out by means of nuclear wave packet propagation on the diabatic electronic PESs, employing a computational method (GridTDSE)[22] that is adept for massive parallel calculations. This technique consists of a direct numerical collocation integration of the 3D time-dependent Schrödinger equation (TDSE):

$$\left[H - i\frac{\partial}{\partial t}\right]\Psi(\boldsymbol{R},t) = 0 \tag{23}$$

where H is the Hamiltonian operator of eqn (19) with the approximation of substituting ${j_z}^2$ by k^2, as discussed in Section 3. The numerical calculation uses a lattice scheme,[34] with the nuclear wave function evaluated at the points of a 3D grid. To incorporate nonadiabatic transitions, the wave function, $\boldsymbol{\Psi}$, is written as a column vector with components $\{\Psi_i\}$, where i labels the (diabatic) electronic states included. The nuclear dynamics on each PES are coupled through the interaction matrix elements $H^d_{ij}(\boldsymbol{R})$, following a procedure similar to that of Ma *et al.*[35] This leads to the matrix equation

$$\boldsymbol{H}^d\boldsymbol{\Psi} = (\boldsymbol{T} + \boldsymbol{V}^d)\boldsymbol{\Psi} = i\dot{\boldsymbol{\Psi}} \tag{24}$$

where $\boldsymbol{V}^d$ stores the values of the potentials at the grid points. $\boldsymbol{T}$, the kinetic energy operator, is a non-diagonal sparse matrix that is obtained by applying the finite differences method (see ref. 34), considering a stencil of 15 points in each dimension.

The calculations were carried out with a grid of 83 points in $R \in [1,11]$ Bohr, 80 points in $r \in [1.3,11]$ Bohr and 73 points in $\theta \in [\varepsilon,\pi-\varepsilon]$ rad, with $\varepsilon = 2 \times 10^{-4}$. In such a numerical

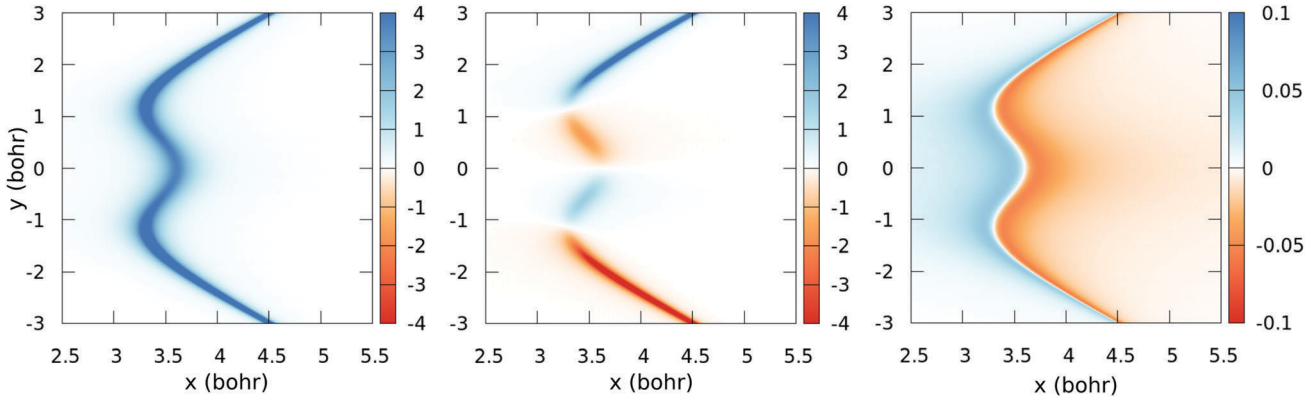

Fig. 7 Colour-map plot of $\partial\gamma_{\tilde{X}\tilde{C}}/\partial x$ (left), $\partial\gamma_{\tilde{X}\tilde{C}}/\partial y$ (middle) and $\partial\gamma_{\tilde{X}\tilde{C}}/\partial\alpha$ (right) as functions of the symmetric (x) and antisymmetric (y) coordinates for $\alpha = 175^{\circ}$. Colour scale values in atomic units.

integration scheme, the singularity at $\theta = 0$ can be eluded by evaluating $\boldsymbol{\Psi}$ on the surroundings of the troublesome points.

The wave function vector components $\{\Psi_i\}$, each one referring to a different PES, were simultaneously propagated in time using a second order difference scheme (SOD), specially adapted to the present case since it conserves norm and energy, accumulating errors only in the phase.[36] The errors are minimized in our calculations by setting the timestep $\Delta t = 0.18$ attosecond (7.5×10^{-3} a.u.), ensuring the stability of the norm and the correct account of the coupling terms between the evolving wave functions on each PES.

To avoid non-physical reflections of the wave function at the grid walls ($L_{max} = 11$ Bohr), we have included a damping function[37] in the propagation scheme. This function leads to a smooth decay of the wave packet for $q > L_{max} - \delta$:

$$M(q) = \begin{cases} e^{-\xi(q-L_{max}+\delta)^2} & \text{if } q > L_{max} - \delta \\ 1 & \text{elsewhere} \end{cases} \quad (25)$$

with $q \equiv (R,r)$, $\delta = 1$ Bohr and $\xi = 0.05$ Bohr^{-2}.

Once the description of the nuclear wave packet in each electronic state is achieved, the integrated probability density $\int_V |\Psi_i(\boldsymbol{r},t)|^2 dV$ represents the time-dependent population of the electronic state i. Such populations can change either due to nonadiabatic transitions among the states included in the model, or due to the dissociating fluxes. The corresponding fragmentation probabilities $\rho_i(t)$ are obtained from the continuity equation in its integral form: $\partial\rho_i/\partial t = \oint_S \boldsymbol{j} \cdot d\boldsymbol{S}$, evaluating the outgoing flux at R, $r = 10.0$ Bohr for the adiabatic components of the wave packet on each electronic state. Finally, the comparison with the experimental measurements is carried out at long times $t > 5$ ps, where the fragmentation probabilities reach asymptotic stable values.

5 Results and discussion

5.1 Franck–Condon initial wave packet

The initial nuclear wave function is built taking the lowest vibrational eigenfunction of the electronic ground state of the water molecule. This PES was obtained with the same procedure and atomic basis set as the electronic states of H_2O^+ described in Section 2. In order to solve the corresponding time-independent Schrödinger equation (TISE), we employed the Lanczos scheme[38] implemented in the GridTDSE code, which is based on the description of Guo *et al.*[39] The analysis of this wave function, when projected over the eigenstates of the adiabatic $\tilde{B}$ PES, shows that it can be described by a wave packet that spans a range of vibrational energies of about 0.1 Hartree, as shown by the vertical Gaussian curve in Fig. 4 for $\theta = 100^{\circ}$. There, the horizontal dashed-lines correspond to the vibrational energies obtained in the adiabatic $\tilde{B}$ PES.

5.2 Effect of increasing the grid-size

As seen in Section 3, CI_2 between the $\tilde{X}$ and $\tilde{C}$ states appears at (R,r) distances between 3 and 5 Bohr. The correct description of the nonadiabatic transitions in the vicinity of this CI requires increasing the grid size from $(R_{max},r_{max}) \approx 7$ Bohr (GRID I[21]) to $(R_{max},r_{max}) \approx 11$ Bohr (GRID II). To check the effect of size-enlargement of the grid on the time-evolution of the electronic state populations, we have reproduced our previous three-state calculation in the new grid. The comparison of the new results

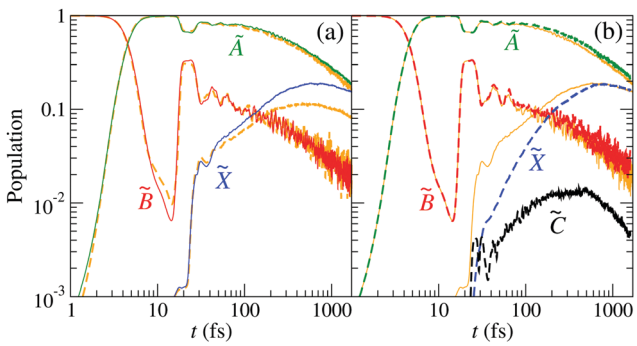

Fig. 8 Population of the electronic states of H_2O^+ (labelled in the panels) as a function of time. (a) The wave packet propagation includes only three electronic states. Dashed-orange lines: grid I with $L_{max} = 7$ Bohr; solid lines: grid II with $L_{max} = 11$ Bohr [see eqn (25)]. (b) The wave packet propagation includes four electronic states (dashed lines) in grid II with $L_{max} = 11$ Bohr. Solid-orange lines are the solid lines of (a).

with those of ref. 21 are presented in Fig. 8(a). There are small differences in the probabilities between both calculations, with small changes in the probabilities, the $\tilde{X}$ state being the more affected.

To study this in more detail, we show in Fig. 9 the sum of the populations of states $\tilde{X}$, $\tilde{A}$ and $\tilde{B}$ for both box-sizes calculations (lines without symbols). As the size of the grid increases, there is a displacement of the population fall towards longer times, due to the damping function acting later. The inset in that figure shows the difference between both calculations, which would correspond to the wave function probability in the extra region. According to this figure, the wave packet enters this region after 50 fs, where it monotonously grows during 800 fs. After that, the amount of wave packet that leaves the extra region exceeds the amount that enters the region from shorter distances and the wave packet in the extra region fades away.

This behaviour can be readily modelled by the free expansion of a 1D wave packet. In this model, we consider the generic wave packet

$$\psi(x,t) = \exp[-\zeta(t)(x - \lambda_1)^2]\sin(\lambda_2 x) \quad (26)$$

where the time-dependent exponential parameter $\zeta(t)$ is introduced to simulate the widening of the wave packet with energy above the dissociation threshold, and

$$\zeta = (\lambda_3 + \lambda_4 t^{\lambda_5})^{-1} \quad (27)$$

With this wave packet, the probability of finding the system in the 1D box of length L can be obtained analytically and is plotted in Fig. 9 for the same grid size as in the three-state calculation, and with parameters (in atomic units) $\lambda_1 = 2.5$, $\lambda_2 = 0.385$, $\lambda_3 = 0.10$, $\lambda_4 = 2.8 \times 10^{-3}$ and $\lambda_5 = 1.2$, obtained to approximately fit the time-dependent probability of the three states of H_2O^+. These results suggest that the expansion of the H_2O^+ wave packet is similar to the free wave packet expansion for the region of the space of coordinates $R,r > 7$ Bohr, as considered in our previous work.

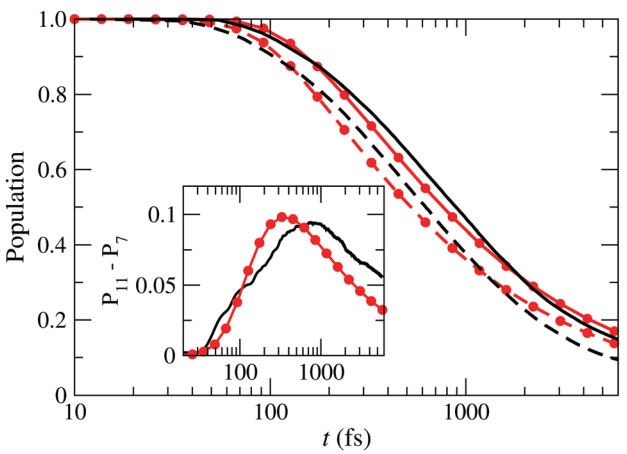

Fig. 9 Sum of the populations of the states $\tilde{X}$, $\tilde{A}$ and $\tilde{B}$ as functions of time for two boxes with L_{max} = 7 Bohr (– – –) and L_{max} = 11 Bohr (—) compared to the probability of finding a particle described by the 1D-wave packet of eqn (26), inside a box with L = 7 Bohr (– • –) and L = 11 Bohr (—•—). Inset: Differences between the populations in the boxes with L = 11 Bohr and L = 7 Bohr for the actual calculation (—) and the 1-D model (—•—).

5.3 Four-state calculation

The initial wave function shown in Section 5.1 was also propagated in the extended grid II with a Hamiltonian matrix that included four electronic states $\{\tilde{X}, \tilde{A}, \tilde{B}, \tilde{C}\}$. Here, the state $\tilde{C}$ is only coupled to $\tilde{X}$ through nonadiabatic couplings described by the transformation angle $\gamma_{\tilde{X}\tilde{C}}$.

The time evolution of the populations of the four electronic states is displayed in Fig. 8(b), for a specific projection of the total angular momentum, K = 1. For an easy comparison, the populations obtained in the three-state calculation, in the same grid, are also included. These results show that state $\tilde{C}$ gets populated at the cost of $\tilde{X}$ at short times, but in the picosecond timescale, the populations of the three- and four-state calculations converge.

As it was shown in ref. 21, the case K = 1 is a representative of the fragmentation probabilities at low temperatures. Here, the $H_2O^+(\tilde{B})$ main fragmentation mechanism remains the same as in the previous three-state calculation: a two-step process in which there is a fast population transfer from $\tilde{B}$ to $\tilde{A}$ in the surroundings of CI_1 and, after 30 fs, a population redistribution and decay through the following reactions:

$$H_2O^+(\tilde{A}) \rightarrow H^+ + OH \quad k_1 \quad (28)$$

$$H_2O^+(\tilde{A}) \rightleftharpoons H_2O^+(\tilde{X}) \quad k_{\pm 2} \quad (29)$$

while the state $\tilde{X}$ dissociates through

$$H_2O^+(\tilde{X}) \rightarrow H + OH^+(^3\Sigma^-) \quad k_3 \quad (30)$$

where k_i are the corresponding reaction constants. States $\tilde{X}$ and $\tilde{C}$ are connected by a CI, and we have

$$H_2O^+(\tilde{X}) \rightleftharpoons H_2O^+(\tilde{C}) \quad k_{\pm 4} \quad (31)$$

while $\tilde{C}$ dissociates through

$$H_2O^+(\tilde{C}) \rightarrow H^+ + OH \quad k_5 \quad (32)$$

The direct fragmentation from $\tilde{B}$ is

$$H_2O^+(\tilde{B}) \rightarrow H + OH^+(^1\Sigma^+) \quad k_6 \quad (33)$$

The probability for fragmentation along each channel is shown in Fig. 10 for the wave packet propagation up to 1600 fs, and these results are used to fit a model for a first-order dissociation mechanism:

$$p_i(t) = r_i(1 - e^{-k_i t}) \quad (34)$$

The parameters obtained by fitting the *ab initio* data from t = 1000 fs to t = 1600 fs are used to draw the thin lines in Fig. 10, and are given in Table 3. There, the fraction of H_2O^+ that remains stable is $r_0 = 1 - r_1 - r_3 - r_5 - r_6$.

In Fig. 8(b), one can note the small populations of state $\tilde{C}$. The differences found in the populations of states $\tilde{A}$ and $\tilde{X}$ by the introduction of state $\tilde{C}$ vanish as t increases, which would eventually lead to similar fragmentation branching ratios. However, one must take into account that we have extended

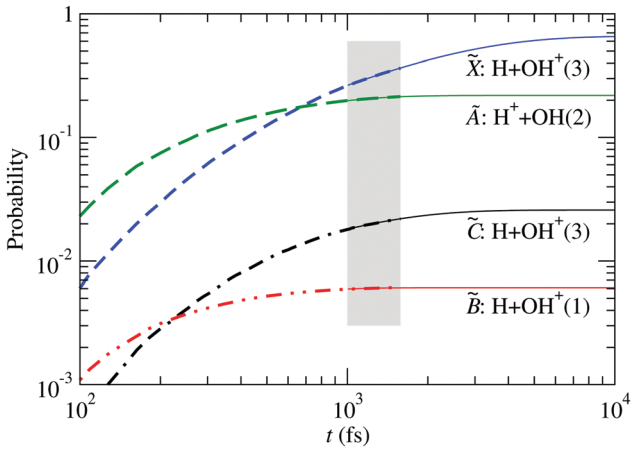

Fig. 10 Fragment probabilities as functions of time in the four-state calculation. Thick-dashed lines: result of the wave packet propagation. Thin-solid lines: fitted model [eqn (34)] using data within the shaded area. The number in brackets indicates the spin multiplicity of the diatomic species. The fitting parameters are given in Table 3.

Table 3 Branching ratios and rate constants for the first-order dissociation dynamics model (34) applied to reactions (28)–(33) of $H_2O^+(\tilde{B})$ and $D_2O^+(\tilde{B})$ fragmentation

	H_2O^+		D_2O^+	
i	r_i	k_i (fs^{-1})	r_i	k_i (fs^{-1})
0	0.091		0.074	
1	0.219	2.4×10^{-3}	0.138	1.3×10^{-3}
3	0.658	5.1×10^{-4}	0.786	6.7×10^{-4}
5	0.026	1.2×10^{-3}	—	—
6	0.006	3.7×10^{-3}	0.002	1.3×10^{-3}

the grid of our previous paper[21] to incorporate transitions in the X̃–C̃ CI. When the grid size is increased, the system remains within the grid limits for a longer time, which, in our calculation, leads to larger populations of states Ã and X̃ with respect to those obtained in our previous three-state work (see Fig. 8(a)).

Ferreira *et al.*[16] have suggested that transitions B̃–C̃ near their PESs crossing might explain their Gaussian structure around 1.8 eV in the H^+ kinetic energy release distribution. However, states B̃ and C̃ are of different symmetry (A′ and A″, respectively) and, correspondingly, their interaction is zero in the Hamiltonian matrix. Also, we note that their leading electronic configurations are $1a_1^2 2a_1^2 1b_2 3a_1^2 1b_1^2$ (B̃) and $1a_1^2 2a_1^2 1b_2^2 3a_1 1b_1 4a_1$ (C̃), which are not linked by one-electron operators, and thus we expect a small B̃–C̃ coupling. Additionally, the fraction of the initial FC wave packet near the crossings (see Fig. 4) is very small. Therefore, we think that this mechanism is unlikely to be competitive with the formation of OH + H^+ *via* B̃–Ã transitions.

5.4 Isotopic effect

Having established in the previous section the small role of state C̃ in the fragmentation ratio, we address the calculation of the branching ratio of a FC wave packet in the B̃ state of D_2O^+ and HDO^+ isotopomers including only three electronic states

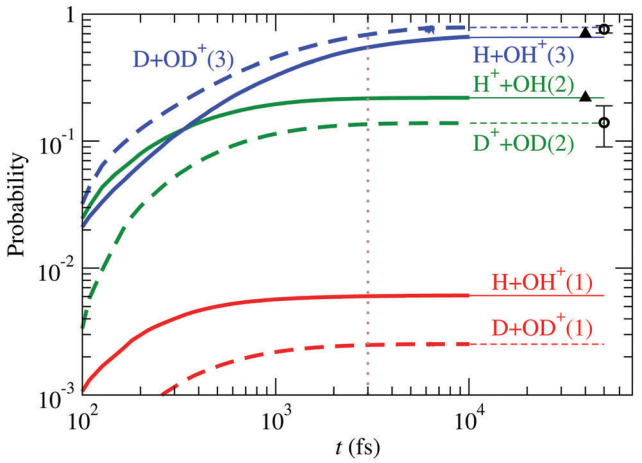

Fig. 11 Comparison between fragmentation probabilities of H_2O^+ and D_2O^+. Circles are the experimental data of Eland[11] for D_2O^+ and triangles those of Tan *et al.*[12] for H_2O^+.

(X̃, Ã and B̃). For D_2O^+, the results are compared with those of H_2O^+ in Fig. 11, also including the experimental data of Eland[11] for D_2O^+ and Tan *et al.*[12] for H_2O^+, in excellent agreement with our calculation. The ratio OD^+/D^+ ($\approx$5.7), larger than that of OH^+/H^+ ($\approx$3.0) (see the values of r_3/r_1 in Table 3), can be understood in terms of kinematic effects: the D_2O^+ wave packet is slower and less spread than the H_2O^+ one, and this is particularly important in the region of linear geometries when the RT coupling transfers part of the wave packet from Ã to X̃. In D_2O^+, the RT coupling is less effective due to the larger reduced mass of the fragments (see eqn (19)), but the slower motion increases the interaction time, which results in a faster increase of the population of X̃ at the expense of Ã, and the consequent increase in the production of OD^+ and decrease of that of D^+.

Turning to the HDO^+ system, it can fragment along four channels: OH^+ + D, OD^+ + H, OH + D^+ and OD + H^+. Here, we start with the FC wave packet as in H_2O^+, and follow its dynamics in the 4 PESs. The fragmentation probabilities are presented in Fig. 12, where they are compared with the coincidence-time-of-flight measurements,[24] and the dynamic parameters of the first order model (34) are given in Table 4. The calculated $\sigma(OD^+)/\sigma(OH^+)$ and $\sigma(H^+)/\sigma(D^+)$ asymptotic ratios are 2.0 and 1.6, respectively, in excellent agreement with the experimental[24] values of 2.1 $\pm$ 0.3 and 1.5 $\pm$ 0.2.

In the calculation, OH^+ and OD^+ are formed through the predissociation of state B̃, which is linked to the single ionization from the $1b_2$ molecular orbital. However, as shown by coincidence experiments,[12] the dissociation into H^+ + OD or D^+ + OH can also take place by one-electron removal from the innermost valence orbital $2a_1$. In fact, the experimental branching ratios of Tan *et al.*[12] show that the cross section for formation of protons in the photoionization of H_2O is given by

$$\sigma(H^+) = 0.22\sigma(1b_2) + 0.74\sigma(2a_1) \quad (35)$$

where $\sigma(1b_2)$ and $\sigma(2a_1)$ are the cross sections for ionization from the molecular orbitals $1b_2$ and $2a_1$, respectively. The experiments[24]

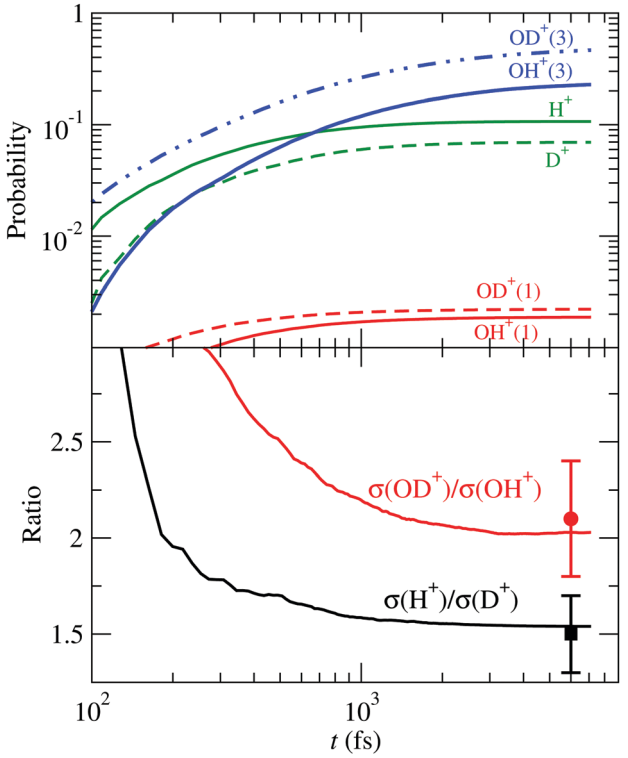

Fig. 12 Upper panel: Fragmentation probabilities of $HDO^+(\tilde{B})$ as functions of time. The numbers in brackets indicate the spin multiplicity of the molecular fragment species. Lower panel: Branching ratios for bond cleavage preference compared with the experimental[24] ones.

Table 4 Branching ratios and rate constants for the first-order dissociation dynamics model (34) applied to the fragmentation of $HDO^+(\tilde{B})$

Fragments	r	k (fs^{-1})
$OD^+(^3\Sigma^-)$ + H	0.47	6.1×10^{-4}
$OH^+(^3\Sigma^-)$ + D	0.23	6.2×10^{-4}
OD + H^+	0.11	1.4×10^{-3}
OH + D^+	0.069	1.3×10^{-3}
$OD^+(^1\Sigma^-)$ + H	0.0022	1.3×10^{-3}
$OH^+(^1\Sigma^-)$ + D	0.0019	1.2×10^{-3}

were carried out at projectile energies of the order of 1 MeV u^{-1}, where the cross sections for ionization from both shells can be estimated by applying the Bethe–Born expression, which leads to similar contributions of the orbitals $1b_2$ and $2a_1$ to the formation of H^+ (see ref. 40). Therefore, the good agreement between our calculation, which only includes the electron removal from $1b_2$, and the experiment, supports the explanation that the ratio $\sigma(H^+)/\sigma(D^+)$ is mainly a kinematic effect,[24] which is common to the wave packet propagation in all electronic PESs.

5.5 Time evolution of an excited vibrational state of $\tilde{B}$

In contrast with the experiment of Tan *et al.*,[12] where the fragmentation of $H_2O^+(\tilde{B})$ ions is recorded just after their formation, in the experiment of Harbo *et al.*,[25] the H_2O^+ ions produced by the ionization of H_2O are stored for a relatively long time; most of the ions undergo fragmentation and only those with an energy below the dissociation threshold survive and are, afterwards, irradiated with a 532 nm (2.33 eV) laser, and the ensuing fragmentation branching ratios measured. The $\tilde{B}$ state only holds two vibrational states below the lowest asymptotic energy of state $\tilde{X}$ and the observed fragmentation was explained as due to the photodissociation of these metastable vibrational states of $\tilde{B}$.

To simulate the experimental[25] conditions, we have time-propagated an initial wave packet that corresponds to the vibrational eigenfunction whose energy lies 2.33 eV above the vibrational ground state in the adiabatic $\tilde{B}$ surface. This vibrational state, whose probability density is shown in Fig. 14, is the seven symmetric stretch overtone. The low-lying vibrational states of the $\tilde{B}$ electronic state have long lifetimes ($\approx$198 μs),[25] which points to ineffective nonadiabatic transitions from those states. Our simulation starts when the interaction of H_2O^+ ions with the laser field ends. Then, the wavefunction of the excited vibrational state has sizeable values around the $\tilde{A}$–$\tilde{B}$ CI and fast nonadiabatic transitions take place, leading to the ion breakdown.

Fig. 13 shows the evolution of this wave packet for $K = 1$, the quantum number for the z-component of the total angular momentum [see eqn (19)]. The comparison of the populations of Fig. 8 with those of Fig. 13(a) clearly shows similar mechanisms, but now there is a larger fragmentation into H^+ + OH, which results in a faster decrease of the population of $\tilde{A}$. This precludes

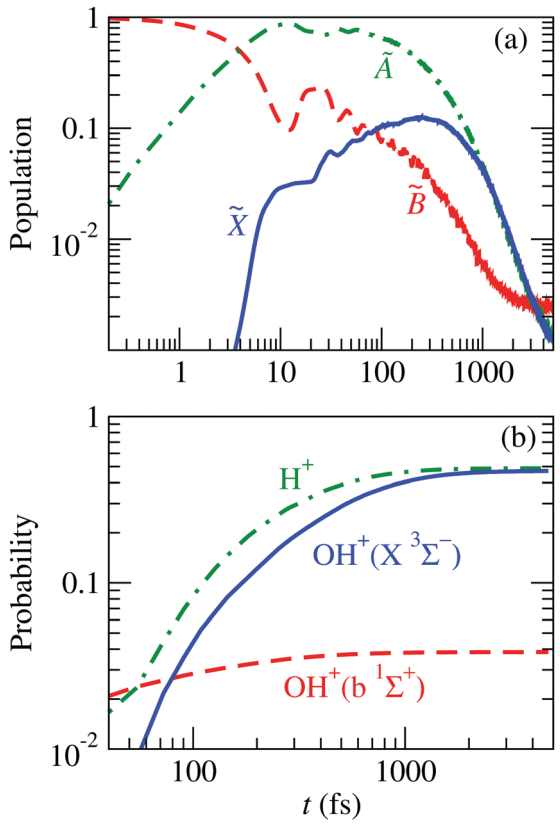

Fig. 13 Time evolution of the nuclear wave packet that is initially equal to the 8th vibrational wave function (given in Fig. 14) of the adiabatic $\tilde{B}$ state. (a) Populations of the electronic states of H_2O^+ indicated in the figure. (b) Probabilities of the possible fragments.

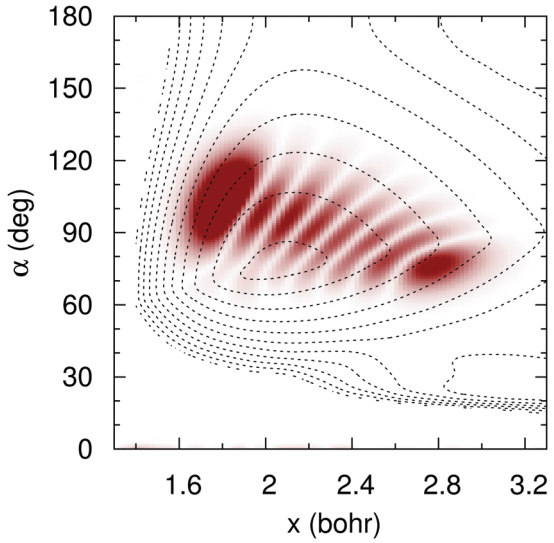

Fig. 14 Wave function probability density (shade) of the seven symmetric stretch overtone in $\tilde{B}$ adiabatic PES (contour dotted lines), for C_{2v} symmetries, as functions of the symmetric coordinate $x = (r_1 + r_2)/2$ and the internal angle α.

the transition to $\tilde{X}$, henceforth a smaller fragmentation into $H + OH^+$; *i.e.*, the initial vibrational excitation leads to a faster motion of the wave packet in the $\tilde{A}$ PES and to the ensuing increase of the k_1 rate constant of reaction (28).

Starting with the excited vibrational state mentioned above, our theoretical fragmentation branching ratio is $\Gamma = \sigma(H^+)/\sigma(OH^+) = 0.96$, in satisfactory agreement with the experimental value[25] of 1.3. Furthermore, our value increases to 1.04, which falls within the ± 0.3 experimental error bars, when considering only the triplet OH^+ species. In both cases, these ratios are considerably larger than the 0.3 ± 0.01 value obtained in the experiments of Tan *et al.*[12] and our theoretical[21] value of 0.33 with the FC initial wave packet.

6 Conclusions

We have carried out the study of the nonadiabatic fragmentation of $H_2O^+(\tilde{B})$ by means of wave packet propagation in four electronic PESs ($\tilde{X}$, $\tilde{A}$, $\tilde{B}$ and $\tilde{C}$), using a modified version of the GridTDSE computational code[22] to simultaneously reproduce the nuclear dynamics on each surface. The values of the potential energy on each electronic state and the nonadiabatic couplings among them were calculated *ab initio* on exactly the same grid of points where the finite difference scheme of the GridTDSE is implemented, enhancing the accuracy of the calculations. This study extends our previous simulations[21] by considering one more electronic state ($\tilde{C}$) and a larger configuration space. Here, we have considered not only an initial FC wave packet, obtained by vertical ionization of H_2O^+ into the $\tilde{B}$ predissociative state of H_2O^+, but also vibrationally excited H_2O^+ ions and the fragmentation of water isotopomers.

The new branching ratio for the fragmentation of $H_2O^+(\tilde{B})$ into $OH + H^+$ and $OH^+ + H$ agrees with previous ($\tilde{X}$, $\tilde{A}$, $\tilde{B}$) three-state calculations,[21] which supports the three-state mechanism. We have also obtained an isotopic dependence of the branching ratio in agreement with the experimental[11,24] data and we have discussed the unlikely role of the $\tilde{B}$–$\tilde{C}$ transitions in the Gaussian peak of the H^+ kinetic energy release measured by Ferreira *et al.*[16]

We have carried out 4-PESs propagation of the initial FC wave packet in the $\tilde{B}$ state of HDO^+. The good agreement between the results of the simulation and the ion–water collision experiments[24] suggests that the cleavage preference found is due to kinematic effects in the evolution of the wave packet in the surfaces that lead to dissociation ($\tilde{A}$ and $\tilde{X}$). Also, we have obtained good agreement with the experiments[11] in the fragmentation branching ratio of $D_2O^+(\tilde{B})$, and explained the differences with respect to the fragmentation of H_2O^+ as due to the larger transitions between $\tilde{X}$ and $\tilde{A}$ states near the linear geometry because of the slower and more compact wave packet in heavy water than in H_2O.

We have also considered the fragmentation of vibrationally excited $H_2O^+(\tilde{B})$ ions to simulate the experimental conditions of Harbo *et al.*[25] We have found that the initial excitation in the symmetric stretch drives the dynamics of the initial wave packet in a way that favors the dissociation from state $\tilde{A}$, leading to branching ratios quite different from those obtained starting with an initial FC-wave packet. In this case, our results agree with the experiments.[25]

Finally, the good agreement between our calculations and the experiments paves the way for the application of this wave packet propagation technique to other three-center systems, see *e.g.* ref. 41.

Conflicts of interest

There are no conflicts of interest to declare.

Acknowledgements

This work has been partially supported by Ministerio de Economía and Competitividad (Spain), project ENE2014-52432-R. The Centro de Computación Científica of UAM is acknowledged for the computational hosting facilities.

References

1 D. A. Neufeld, J. R. Goicoechea, P. Sonnentrucker, J. H. Black, J. Pearson, S. Yu, T. G. Phillips, D. C. Lis, M. De Luca, E. Herbst, P. Rimmer, M. Gerin, T. A. Bell, F. Boulanger, J. Cernicharo, A. Coutens, E. Dartois, M. Kazmierczak, P. Encrenaz, E. Falgarone, T. R. Geballe, T. Giesen, B. Godard, P. F. Goldsmith, C. Gry, H. Gupta, P. Hennebelle, P. Hily-Blant, C. Joblin, R. Kołos, J. Krełowski, J. Martín-Pintado, K. M. Menten, R. Monje, B. Mookerjea, M. Perault, C. Persson, R. Plume, M. Salez, S. Schlemmer, M. Schmidt, J. Stutzki, D. Teyssier, C. Vastel, A. Cros, K. Klein, A. Lorenzani, S. Philipp, L. A. Samoska, R. Shipman, A. G. G. M. Tielens, R. Szczerba and J. Zmuidzinas, *Astron. Astrophys.*, 2010, **521**, L10.

2 E. González-Alfonso, J. Fischer, S. Bruderer, H. S. P. Müller, J. Graciá-Carpio, E. Sturm, D. Lutz, A. Poglitsch, H. Feuchtgruber, S. Veilleux, A. Contursi, A. Sternberg, S. Hailey-Dunsheath, A. Verma, N. Christopher, R. Davies, R. Genzel and L. Tacconi, *Astron. Astrophys.*, 2013, **550**, A25.
3 R. Wayne, *Chemistry of Atmospheres: An Introduction to the Chemistry of the Atmospheres of Earth, the Planets, and Their Satellites*, Oxford University Press, 2000.
4 M. A. Disanti, U. Fink and A. B. Schultz, *Icarus*, 1990, **86**, 152–171.
5 S. A. Fuselier, K. Altwegg, H. Balsiger, J. J. Berthelier, A. Bieler, C. Briois, T. W. Broiles, J. L. Burch, U. Calmonte, G. Cessateur, M. Combi, J. De Keyser, B. Fiethe, M. Galand, S. Gasc, T. I. Gombosi, H. Gunell, K. C. Hansen, M. Hässig, A. Jäckel, A. Korth, L. Le Roy, U. Mall, K. E. Mandt, S. M. Petrinec, S. Raghuram, H. Rème, M. Rinaldi, M. Rubin, T. Sémon, K. J. Trattner, C.-Y. Tzou, E. Vigren, J. H. Waite and P. Wurz, *Astron. Astrophys.*, 2015, **583**, A2.
6 C. R. Brundle and D. W. Turner, *Proc. R. Soc. London, Ser. A*, 1968, **307**, 27–36.
7 J. E. Reutt, L. S. Wang, Y. T. Lee and D. A. Shirley, *J. Chem. Phys.*, 1986, **85**, 6928–6939.
8 S. Truong, A. Yencha, A. Juarez, S. Cavanagh, P. Bolognesi and G. King, *Chem. Phys.*, 2009, **355**, 183–193.
9 A. Lorquet and J. Lorquet, *Chem. Phys.*, 1974, **4**, 353–367.
10 M. Eroms, M. Jungen and H.-D. Meyer, *J. Phys. Chem. A*, 2010, **114**, 9893–9901.
11 J. Eland, *Chem. Phys.*, 1975, **11**, 41–47.
12 K. Tan, C. Brion, P. V. der Leeuw and M. van der Wiel, *Chem. Phys.*, 1978, **29**, 299–309.
13 I. Powis and D. J. Reynolds, *J. Chem. Soc., Faraday Trans.*, 1991, **87**, 921–926.
14 K. Norwood, A. Ali and C. Y. Ng, *J. Chem. Phys.*, 1991, **95**, 8029–8037.
15 A. L. F. de Barros, J. Lecointre, H. Luna, M. B. Shah and E. C. Montenegro, *Phys. Rev. A*, 2009, **80**, 012716.
16 N. Ferreira, L. Sigaud and E. C. Montenegro, *Phys. Rev. A*, 2017, **96**, 012705.
17 N. Ferreira, L. Sigaud and E. C. Montenegro, *J. Phys. Chem. A*, 2017, **121**, 3234–3238.
18 M. Paniagua, R. Martínez, P. Gamallo and M. González, *Phys. Chem. Chem. Phys.*, 2014, **16**, 23594–23603.
19 R. Martínez, M. Paniagua, J. Mayneris-Perxachs, P. Gamallo and M. González, *Phys. Chem. Chem. Phys.*, 2017, **19**, 3857–3868.
20 P. Gamallo, P. Defazio, M. González, M. Paniagua and C. Petrongolo, *Phys. Chem. Chem. Phys.*, 2015, **17**, 23392–23402.
21 J. Suárez, L. Méndez and I. Rabadán, *J. Phys. Chem. Lett.*, 2015, **6**, 72–76.
22 J. Suarez, S. Farantos, S. Stamatiadis and L. Lathouwers, *Comput. Phys. Commun.*, 2009, **180**, 2025–2033.
23 I. Ben-Itzhak, A. M. Sayler, M. Leonard, J. Maseberg, D. Hathiramani, E. Wells, M. Smith, J. Xia, P. Wang, K. Carnes and B. Esry, *Nucl. Instrum. Methods Phys. Res., Sect. B*, 2005, **233**, 284–292.
24 A. M. Sayler, M. Leonard, K. D. Carnes, R. Cabrera-Trujillo, B. D. Esry and I. Ben-Itzhak, *J. Phys. B: At., Mol. Opt. Phys.*, 2006, **39**, 1701.
25 L. S. Harbo, S. Dziarzhytski, C. Domesle, G. Brenner, A. Wolf and H. B. Pedersen, *Phys. Rev. A*, 2014, **89**, 052520.
26 H.-J. Werner, P. J. Knowles, G. Knizia, F. R. Manby and M. Schütz, *WIREs Comput. Mol. Sci.*, 2012, **2**, 242–253.
27 T. H. Dunning Jr., *J. Chem. Phys.*, 1989, **90**, 1007–1023.
28 D. Elizaga, L. F. Errea, A. Macías, L. Méndez, A. Riera and A. Rojas, *J. Phys. B: At., Mol. Opt. Phys.*, 1999, **32**, L697.
29 P. Barragán, L. F. Errea, A. Macías, L. Méndez, I. Rabadán, A. Riera, J. M. Lucas and A. Aguilar, *J. Chem. Phys.*, 2004, **121**, 11629–11638.
30 D. J. Haxton, T. N. Rescigno and C. W. McCurdy, *Phys. Rev. A*, 2007, **75**, 012711.
31 D. J. Haxton, T. N. Rescigno and C. W. McCurdy, *Phys. Rev. A*, 2007, **76**, 049907(E).
32 C. Leforestier, *J. Chem. Phys.*, 1991, **94**, 6388–6397.
33 S. Carter and N. Handy, *Mol. Phys.*, 1984, **52**, 1367–1391.
34 R. Guantes and S. C. Farantos, *J. Chem. Phys.*, 1999, **111**, 10827–10835.
35 J. Ma, C. Xie, X. Zhu, D. R. Yarkony, D. Xie and H. Guo, *J. Phys. Chem. A*, 2014, **118**, 11926–11934.
36 C. Leforestier, R. Bisseling, C. Cerjan, M. Feit, R. Friesner, A. Guldberg, A. Hammerich, G. Jolicard, W. Karrlein, H.-D. Meyer, N. Lipkin, O. Roncero and R. Kosloff, *J. Comput. Phys.*, 1991, **94**, 59–80.
37 D. Dundas, J. F. McCann, J. S. Parker and K. T. Taylor, *J. Phys. B: At., Mol. Opt. Phys.*, 2000, **33**, 3261.
38 C. Lanczos, *J. Res. Natl. Bur. Stand., Sect. B*, 1950, **45**, 255–282.
39 H. Guo, R. Chen and D. Xie, *J. Theor. Comput. Chem.*, 2002, **01**, 173–185.
40 C. Illescas, L. F. Errea, L. Méndez, B. Pons, I. Rabadán and A. Riera, *Phys. Rev. A*, 2011, **83**, 052704.
41 A. D. Smith, E. M. Warne, D. Bellshaw, D. A. Horke, M. Tudorovskya, E. Springate, A. J. H. Jones, C. Cacho, R. T. Chapman, A. Kirrander and R. S. Minns, *Phys. Rev. Lett.*, 2018, **120**, 183003.